JGR Oceans

RESEARCH ARTICLE

10.1029/2023JC020743

Trough-Scale Slope Countercurrent Over the East China Sea Continental Slope Driven by Upwelling Divergence

Xuan Cui[1,2,3], **Dezhou Yang**[1,2,3,4], **Arthur J. Miller**[5], **Baoshu Yin**[1,2,3,4], **and Jiayan Yang**[6]

[1]Key Laboratory of Ocean Observation and Forecasting, Key Laboratory of Ocean Circulation and Waves, Institute of Oceanology, Chinese Academy of Sciences, Qingdao, China, [2]Laboratory for Ocean Dynamics and Climate, Qingdao Marine Science and Technology Center, Qingdao, China, [3]CAS Engineering Laboratory for Marine Ranching, Institute of Oceanology, Chinese Academy of Sciences, Qingdao, China, [4]College of Marine Sciences, University of Chinese Academy of Sciences, Beijing, China, [5]Scripps Institution of Oceanography, University of California San Diego, La Jolla, CA, USA, [6]Department of Physical Oceanography, Woods Hole Oceanographic Institution, Woods Hole, MA, USA

Key Points:

- Over the entire East China Sea continental slope, the slope countercurrent beneath the surface Kuroshio Current is potentially continuous
- The slope countercurrent is the western part of a deep cyclonic circulation in the Okinawa Trough
- The upwelling divergence along the East China Sea continental slope is the main forcing mechanism of the slope countercurrent

Correspondence to:

D. Yang and B. Yin,
yangdezhou@qdio.ac.cn;
bsyin@qdio.ac.cn

Citation:

Cui, X., Yang, D., Miller, A. J., Yin, B., & Yang, J. (2024). Trough-scale slope countercurrent over the East China Sea continental slope driven by upwelling divergence. *Journal of Geophysical Research: Oceans*, *129*, e2023JC020743. https://doi.org/10.1029/2023JC020743

Received 1 DEC 2023
Accepted 12 SEP 2024

Author Contributions:

Conceptualization: Xuan Cui, Dezhou Yang
Funding acquisition: Dezhou Yang
Investigation: Xuan Cui
Methodology: Xuan Cui
Supervision: Dezhou Yang, Arthur J. Miller, Baoshu Yin, Jiayan Yang
Validation: Xuan Cui
Visualization: Xuan Cui
Writing – original draft: Xuan Cui
Writing – review & editing: Xuan Cui, Dezhou Yang, Arthur J. Miller, Baoshu Yin, Jiayan Yang

Abstract

Observations have revealed the existence of persistent slope countercurrents (SCCs) that flow southwestward beneath the Kuroshio Current at several locations over the East China Sea (ECS) continental slope. It was not clear whether these flows are localized circulation features or segments of a trough-scale circulation system in the Okinawa Trough (OT). We demonstrate that there indeed exists a potentially continuous trough-scale SCC along the ECS slope that is associated with an OT-wide cyclonic circulation using high-resolution model simulations and physical interpretations. The detailed features of the deep OT circulation are illustrated by the trajectories of the Lagrangian drifters and the time-varying distributions of passive tracers. The SCC in the ECS is characterized by its weak yet persistent nature, typically located in narrow sloping regions at the isopycnal layer of 26.6–27.3 kg m^{-3}. It exhibits a characteristic speed of approximately O-(1) cm s^{-1}. Analyses and experiments suggest that the divergence of upwelling in the SCC layer (26.6–27.3 σ_θ surface) gives rise to lateral potential vorticity transport, ultimately driving the deep cyclonic circulation. Furthermore, the SCC also displays a substantial connection with the onshore intrusion of the Kuroshio Current, particularly to the northeast of Taiwan Island. The SCC may potentially play a crucial role in the transport of heat and nutrients, as well as in regulating sediment distributions within the deep OT. This mechanism offers fresh insights into explaining the presence of undercurrents in semi-enclosed marginal seas.

Plain Language Summary

The Okinawa Trough (OT) is a key link between the Pacific Ocean and the East China Sea (ECS) continental shelf. It was observed by previous studies that persistent southwestward slope countercurrents (SCCs) exist beneath the northeastward Kuroshio Current at several locations over the ECS continental slope. These countercurrents have been attributed to a variety of mechanisms based on analyses and interpretations of observations made at different locations. It is yet not clear whether these flows are localized circulation features or segments of an OT-wide circulation system. In this study, we find that there indeed exists a trough-scale SCC along the ECS slope that is associated with an anti-clockwise circulation. Analyses indicate the OT experiences different vertical volume exchanges at the deep layer, which induces lateral exchanges of potential vorticity (a dynamically conserved quantity in an ideal and rotating fluid) and eventually drives the SCC. Numerical experiments are performed to show the validity of this process. The SCC may be of vital importance in transporting heat and nutrients and regulating the sediment distributions in the OT. This mechanism is potentially applicable to explain the undercurrent in similar semi-enclosed marginal seas.

1. Introduction

The global ocean circulation system is spatially complex and temporally evolving. Many of its aspects remain insufficiently understood, especially in the deep ocean beneath the main thermocline where direct observations are still sparse. Despite varying dynamics, deep currents that counter surface currents are observed, and the reversal of flow from the surface to the bottom is a common phenomenon in both open oceans and marginal seas. The deep circulation in the Atlantic Ocean is most typical. Stommel (1958) and Stommel and Arons (1960a, 1960b) constructed the first conceptual model of abyssal circulation in their attempt to explain how the North Atlantic Deep Water is exported away from its formation sites in the subpolar North Atlantic Ocean. It is postulated that deep western boundary currents must play a critical role in transporting water masses meridionally, which has been confirmed by subsequent observations (e.g., Toole et al., 2017; Warren & Speer, 1991) in

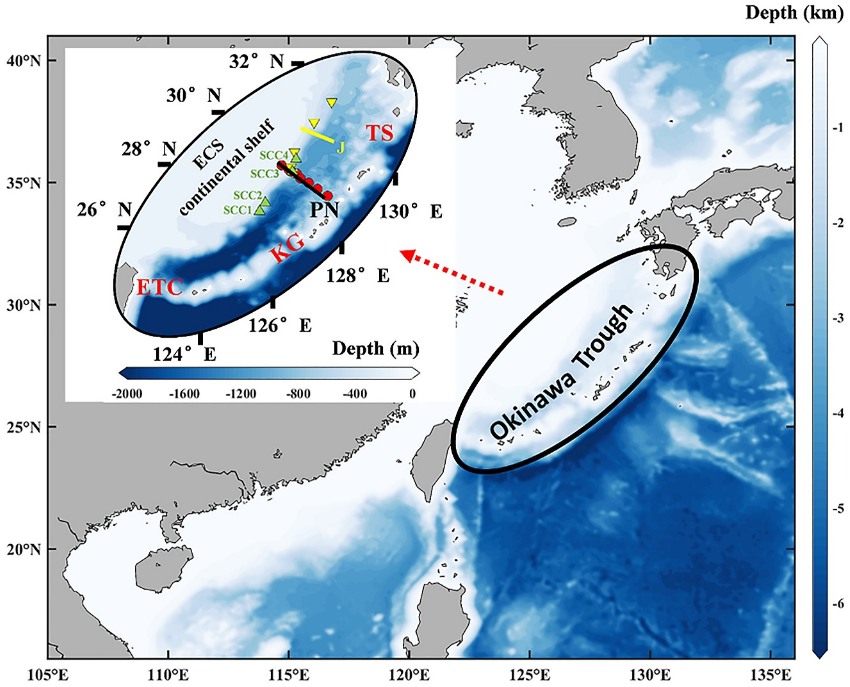

Figure 1. Geographical setting and model domain. The black ellipse delineates the research domain, encompassing the East China Sea slope and the Okinawa Trough. The PN transect is marked with a black solid line. Some of the previous mooring locations are marked: the yellow downward triangles from Lie et al. (1998); the green upward triangles from Nakamura et al. (2008); the red dots from Andres et al. (2008). The yellow line marks the J line from Lie et al. (1998) where the Kuroshio path leaves the continental slope southwest of Kyushu and strong upwelling exists. The deep channel linking the Okinawa Trough and the Pacific Ocean is highlighted with red characters: ETC, east Taiwan channel; KG, Kerama Gap; TS, Tokara Strait.

the Atlantic Ocean and elsewhere (e.g., Andres et al., 2015; Beal & Bryden, 1997). In semi-enclosed marginal seas, the flow reversal structures are sometimes more complicated. Studies have shown the multi-layer circulation structure in the South China Sea (Gan et al., 2016; Zhu et al., 2017) and the Banda Sea (Zhu et al., 2019). Understanding these stratified circulation is most important yet challenging because of the limited observation.

The abyssal ocean circulation in the North Pacific Ocean is distinctly different from that in the North Atlantic Ocean because of a lack of deep-water formation. Observations, however, have revealed the existence of the slope countercurrents (SCCs) flowing southwestward over the ECS continental slope beneath the northeastward flowing Kuroshio Current (see Figure 1 for the mooring locations). Lie et al. (1998) were the first to identify and actually name this current. Their analyses of mooring observations revealed a quasi-permanent SCC in the northern Okinawa Trough (OT) and a wave-like SCC feature in the central OT. They attributed the SCC formation mechanism in the northern and central OT to the upwelling associated with the Kuroshio Current branching and the frontal eddies. The SCC is also observed in an inverted echo sounder array by James et al. (1999) where the velocity maximum is located at 800-m depth. Nakamura et al. (2003, 2008) concluded that the SCC is relatively stronger and deeper in the southern basin of northern OT than in the northern basin and its variability is highly influenced by the Kuroshio path meander. As for the SCC mechanism in the northern OT, Nakamura et al. (2008) suggested that based on analyses of numerical model simulations, deep cyclonic eddies are the main cause of the observed countercurrent. Based on a 23-month acoustic Doppler current profiler observation, Andres et al. (2008) also showed the existence of the SCC at the PN line in the ECS. Due to the lack of simultaneous observations in the OT and the limited understanding of the deep ocean circulation, southwestward flows beneath the Kuroshio Current at different observing sites have been considered as parts of localized circulations that are attributable to local processes. For example, Nakamura et al. (2021, 2008) and Nakamura (2005) proposed that the SCC observed in the northern OT is a consequence of baroclinic instability originating from the surface Kuroshio front. Additionally, they believe the presence of SCC in the southern part is attributed to the persistent inflow of intermediate and deep water from the Kerama Gap (Nakamura et al., 2013;

Nishina et al., 2016). More systematic analyses of the OT-wide dynamical processes are needed so that a better understanding on the driving mechanism of SSC, either local or basin-wide, can be developed.

In semi-enclosed deep basins, the sense boundary flows are strongly constrained by the lateral fluxes of the potential vorticity (PV) (Yang & Price, 2000, 2007). A positive PV transport would require a cyclonic circulation along the boundary so that the frictional PV transport balances the lateral advective PV transport. This PV integral constraint has been applied to explain deep circulations in several marginal seas, such as in the Arctic Ocean (Karcher et al., 2007; Yang, 2005), and the South China Sea (Gan et al., 2016; Lan et al., 2013; Zhu et al., 2017). The OT is a semi-enclosed basin with several openings for the deepwater layer and the SCC can be considered as the northwestern part of the deep cyclonic circulation within the OT.

A trough-scale circulation may profoundly regulate mass transport and play an important role in deep-ocean carbon cycling. Furthermore, the trough-scale annual-mean circulation obtained by numerical model calculation and its formation mechanism are crucial for better understanding of the potential continuity of the SCC observed at several sites in the OT. The results of this study are expected to contribute better comprehending of the complex observational results in the ECS.

The remainder of the paper is structured as follows. Section 2 offers a brief introduction to the numerical model, encompassing its configuration, validation, and the inclusion of drifters and tracers. In Section 3, a comprehensive discussion of the circulation features is presented through analyses of our model results. The formation mechanism of the SCC is outlined and validated in Section 4. The discussion part Section 5 incorporates relevant features and future research interests. Finally, Section 6 provides concluding remarks.

2. Numerical Model

2.1. Model Setup

The numerical model in this study is based on the Regional Ocean Model System (ROMS), a free-surface, terrain-following, primitive equation ocean model (Dinniman et al., 2003; Marchesiello et al., 2003; Peliz et al., 2003; Shchepetkin & McWilliams, 2005; Song & Haidvogel, 1994). ROMS has been widely used in various oceanographic studies. Detailed information about the model can be found in the works of Shchepetkin and McWilliams (2003, 2005).

In this study, we use the ECS-SCS ocean model (ESOM) from Yang, Huang, et al. (2018) to simulate climatological ocean circulation in the OT (see Figure 1 for the model domain). Extending from 105°E to 136°E and from 15°N to 41°N, ESOM has a horizontal resolution of 3´ × 3´(-5 km) and 31 vertical layers. As shown in Figure 1, the OT is deep and narrow. It is worth noting that the maximum grid stiffness ratios, $rx0 = 1.62$ (Haney, 1991) and $rx1 = 3.72$ (Beckmann & Haidvogel, 1993), which suggests ESOM grids are fine enough to reflect the steep slope topography without causing instability problems or spurious deep currents. In addition, climatological monthly mean ERA-Interim reanalysis wind stress with an original time span of 12 hr (Dee et al., 2011) is used to force the Nest2 model, river fluxes of the Yangtze River and the Pearl River (http://xxfb.hydroinfo.gov.cn) and 10 tidal components from the TPXO7 (Egbert & Erofeeva, 2002) are included in ESOM. Atmosphere forcings are utilized from COADS data (Diaz et al., 2002). Feeds by the open boundary conditions from a larger grid domain (fully spun up to cover the Anderson and Gill timescale) including the whole Pacific Ocean, ESOM has been consistently integrated for 15 years for the spin-up process. The 15th-year output from the spun-up ESOM is utilized to analyze the circulation features over the ECS continental slope. All the configuration details can be accessed in Yang, Yin, et al. (2018).

2.2. Model Validation

ESOM has undergone rigorous validation, consistently demonstrating strong agreement with the observations available in previous studies on ocean circulations in the ECS regions (Yang, Huang, et al., 2018; Yang et al., 2020), such as the Kuroshio Current, the Taiwan Warm Current, and the Tsushima Warm Current. ESOM also performs well in regions with steep and complex topography where Kuroshio onshore intrusions often take place (Cui et al., 2021).

Although ESOM output was intensively checked in previous studies, we execute an extra model validation by comparing the velocity structure at the well-studied PN line with accessible observations (Andres et al., 2008).

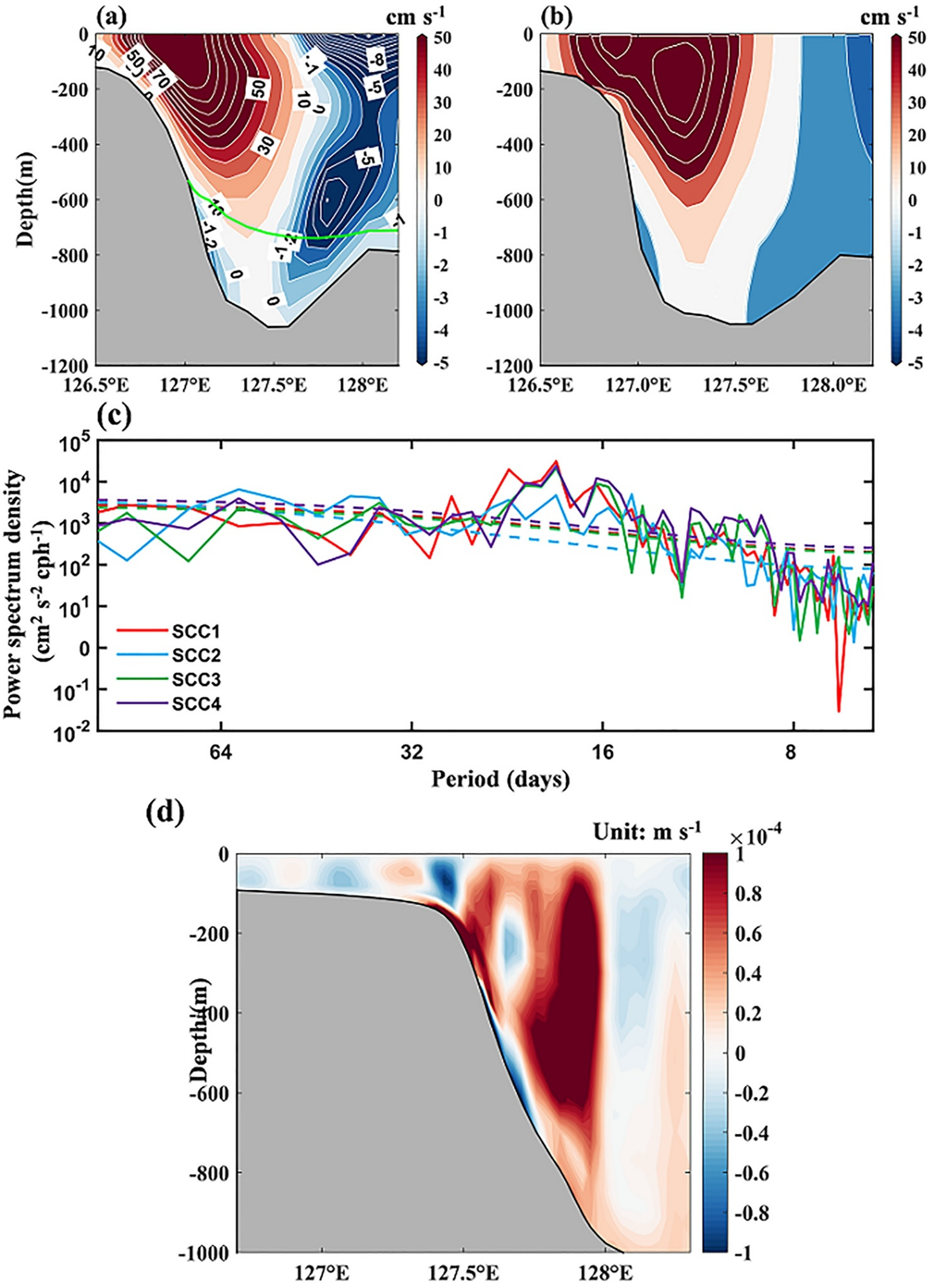

Figure 2. Annual mean cross-transect velocity at the PN line from the model output (a and b) observations reconstructed from Andres et al. (2008). The green line is the 26.6 σ_θ surface. Northeastward positive, unit: cm s^{-1}. The contour intervals are different for positive and negative values. (c) Power spectrum of the along-slope velocities at SCC1-SCC4 (solid line), the dashed lines reflect 95% confidence levels. (d) The modeled annual mean vertical velocity at the J line.

Figure 2a shows the velocity across the section along the well-studied PN line in the control run. In the upper layer, the most significant feature is the northeastward Kuroshio Current. The Kuroshio Counter Current (KCC), which flows southwestward, can be observed on the east side of the Kuroshio Current. The horizontal velocity structure aligns with the velocity profile across a Munk frictional boundary layer, as described by Pedlosky (1979) and Qiu and Imasato (1990). Significantly, it distinctly illustrates the presence of the SCC beneath the core of the Kuroshio Current, the typical velocity of which is about O- (1) cm $\cdot$ s^{-1}. The envelope of the SCC turns to emerge in the deep layer beneath the 26.6 potential density (σ_θ) surface. Overall, the modeled velocity structure along the

PN line closely resembles the observational pattern depicted in Figure 2b. However, there are slight discrepancies in the detailed intensity: the double core structure observed by Andres et al. (2008) is absent, and the intensity of the KCC is generally weaker but the KC is much stronger in the ESOM model results than observational results.

Previous studies have highlighted the importance of frontal eddies generated near the Kuroshio path in inducing upwelling and onshore intrusions (e.g., Isobe & Beardsley, 2006; Yanagi et al., 1998). These processes are thought to be closely related to the presence and variability of the local southwestward flows. Here we operated power-spectrum analysis on the modeled time series of the along-slope velocity at the same locations (SCC1-SCC4 in Figure 1) with those in Nakamura et al. (2008). Despite being a climatological simulation, ESOM still reveals a significant period band around 10–20 days that stands out from the background noise (Figure 2c). This period band is typical for frontal eddies (Ichikawa & Beardsley, 1993; James et al., 1999; Qiu et al., 1990; Sugimoto et al., 1988), although the power density is much weaker than that reported in Nakamura et al. (2008) from ADCP mooring observations.

ESOM successfully reproduces the strong upwelling over the ECS continental slope as well. As shown in Figure 2d, the strong upwelling along the J line aligns with the dome-like structure of temperature and salinity reported by Lie et al. (1998). This alignment is largely due to the Kuroshio path moving away from the continental slope, resulting in strong divergence in the upwelling region.

From the above-mentioned comparisons of model results with observational results, it can be concluded that the ESOM is acceptable to be an appropriate tool for the purpose of studying the SCC formation mechanism, which is associated with the mean-state pattern.

2.3. Lagrangian Drifters and Passive Tracers

To grasp the characteristics of the SCC, three-dimensional Lagrangian drifters are strategically released in ESOM. Unlike isobaric and geopotential drifters, these Lagrangian drifters are designed to accurately capture the genuine movement of water particles, with their three-dimensional positions computed by integrating $d\boldsymbol{X_i}/dt = \boldsymbol{u}$ at each time step, where X_i is the location of each drifter, $\boldsymbol{u} = \boldsymbol{u}(x, y, z, t)$ is the three-dimensional current velocity. These drifters are massless, meaning they do not possess inertia and will therefore move along with the background current during the model simulation.

Passive tracers (which do not contribute to the equations of motion) are also released within the OT to gauge the mass transport of deep currents. Distinct from temperature and salinity, they are considered as additional tracers which are computed through the integration of the tracer equation (Shchepetkin & McWilliams, 2005). There are generally two ways to introduce tracers into numerical simulations. One approach involves specifying a tracer distribution at the initial state, integrating it over time, and observing the resulting concentration as it plays out; the alternative method, which is applied in this study, involves continuously dying specific parts of the water column with tracers at a particular concentration, effectively designating these locations as point sources for tracers. Apart from temperature and salinity, we additionally introduce a group of point-source passive tracers into the model computation. This technique has been utilized by a group of studies (Hu et al., 2020; Isobe & Beardsley, 2006; Yang, Huang, et al., 2018).

These drifters and tracers are released at an annual-mean ESOM simulation, effectively damping multiscale variabilities that could potentially disrupt the potential continuity of the SCC.

3. Circulation Features in the Deep OT

3.1. Continuity

The question of whether the SCCs over the ECS continental slope are spatially continuous arises from their consistent presence at several locations in previous studies. Therefore, the potential continuity of the SCC is investigated by releasing Lagrangian drifters in ESOM. A total of 100 drifters are initially positioned at an upstream section S0 (see its location in Figure 3a), focusing specifically on the SCC core to mitigate the influence of bottom eddies, which could potentially affect the SCC in advecting these drifters. This core is characterized by velocities greater than 1.5 cm s^{-1} and is situated along the northern slope of the ECS around 30.5°N. The flow pattern in Figure 3b clearly indicates the existence of the southwestward current in continental slope in the northern OT,

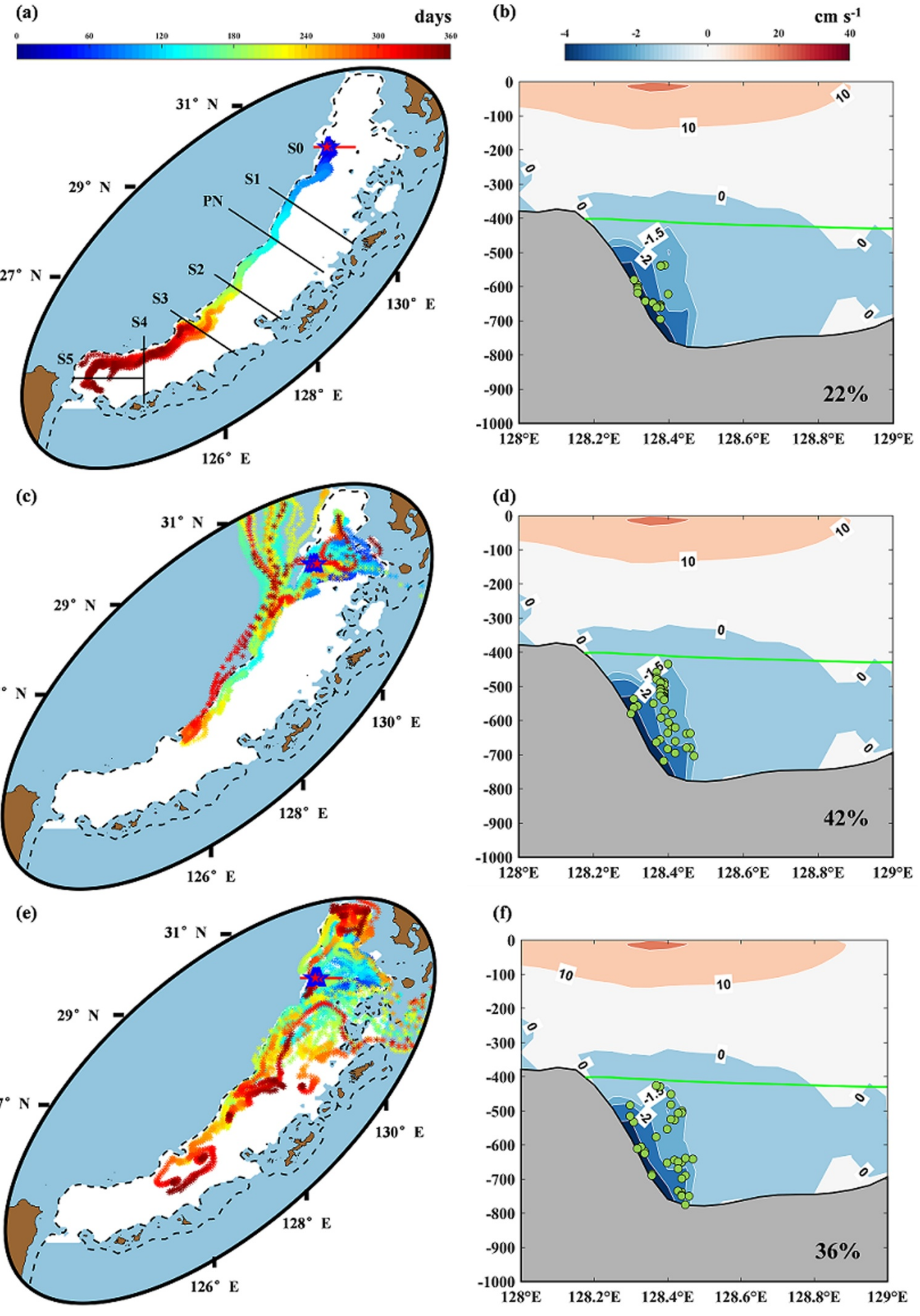

Figure 3. Different trajectory categories of drifters released in the northern Okinawa Trough. The left panels illustrate the time-varying locations, with the black dashed line representing the 500-m isobaths, the red line indicating the location of the releasing transect, and the red stars marking the initial locations. Regions shallower than the depth minimum of the 26.6 σ_θ surface or beyond the Okinawa Trough are masked with blue shading. The right panels display the along-slope velocity structure, with green dots indicating the releasing locations. The contour intervals are different for positive and negative values.

where the Kuroshio Current is not present. Released on the first day of January, these drifters are tracked for 360 days and are recorded every 36 hr.

Although the deep circulation is extremely complex with numerous details, the trajectories of these drifters share some similarities, and the envelope of the SCC is intricately sculptured by the trajectories of the Lagrangian drifters. Three groups of drifters are summarized, with their trajectories represented by colored asterisks in Figure 3. The trajectories of the drifters are categorized in terms of their fates (see their trajectories in Figures 3a, 3c, and 3e and initial locations in Figures 3b, 3d, and 3f). It is worth mentioning that 22 out of 100 drifters (group 1) travel southwestward along the steep ECS continental slope (depicted by the 500-m isobath on the western OT) during the whole tracking period (Figure 3a). What is even more interesting is that these drifters are initially released closer to the velocity maximum of the SCC. The percentage of group 1 exceeds 50% when the drifters released in regions with a velocity exceeding 2 cm s^{-1} are taken into account, which reveals that drifters released close to the velocity maximum are more likely to follow the SCC mainstream and be advected southwestward.

The presence and the potential continuity of SCC along the ECS slope are further illustrated by six extra cross-shelf transects. We choose six representative transects over the entire ECS slope to show the previously observed SCCs are not localized circulation features but rather a spatially continuous circulation over the ECS continental slope. Figures 4a–4f depict the normal velocity across transects S1, PN, and S2 to S5 with the locations of the group 1 drifters when they pass through them, the locations of group 1 drifters further confirm that the drifters remain within the SCC core. After a 1-year traveling time, these drifters are capable of reaching the steep topography northeast of Taiwan Island and 11 of them even make it to the very southern section S5. Additionally, the circulation within the sloping area is characterized by a southwestward current, flowing counter to the direction of the surface Kuroshio Current. Another characteristic of the SCC is the deepening of its core during its downstream evolution, which starts from ~700 m at S0 to ~1,100 m at S5 (Figures 4a–4f), which may be attributed to the deepening downstream bottom topography. Although the SCC exhibits spatial variations in terms of depth range, width, and velocity maximum, it is predominantly confined to the 26.6–27.3 σ_θ surfaces throughout the ECS slope. Therefore, based on the velocity stratification (Figure 4g) and the continuity shown by the group 1 drifters, we select the layer with 26.6–27.3 σ_θ as the SCC layer.

That being said, the other drifters, which are typically released in regions slightly further from the velocity maximum, exhibit different behaviors by leaving the core halfway through and ending up traveling with other background flows. Specifically, 42% can still be advected southwestward by the background SCC, however, they tend to be transported upward more easily upon reaching upwelling active regions and subsequently penetrating onto the ECS shelf (group 2, see Figures 3c and 3d). These trajectories effectively reflect the strong upwelling and active onshore intrusion over the ECS continental slope. The remaining 36% leave the SCC midway, tend to be carried by the Kuroshio Current, and eventually disperse randomly in the OT (group 3, see Figures 3e and 3f). It is worth noting that the ability of the SCC to retain these drifters is weak; they can be displaced from the SCC core with perturbations as they are transported southwestward, even if initially released at the core of the SCC. The flow patterns at each section and the trajectories emphasize the weak, narrow, but continuous nature of the SCC.

3.2. Onshore Intrusion and Upwelling Divergence

The ECS continental slope has been widely documented as a location where onshore intrusions of Kuroshio water occur, characterized by high-salinity and nutrient-rich content (Gan et al., 2016; Hu et al., 2020; Isobe & Beardsley, 2006; Wei, 2018; Yang, Huang, et al., 2018). Onshore intrusion refers to the movement of water particles toward shallower regions and is invariably accompanied by vertical displacements of their altitudes. The vertical displacements of water particles are evident in the drifter trajectories which signifies the active onshore intrusion at the central and northern part of the ECS slope.

To include more details on the onshore intrusion and the upwelling in the SCC layer, the water within the 26.6–27.3 σ_θ surface is dyed with passive tracers with a fixed 100 kg m^{-3} concentration which serve as point sources in the OT (Figure 5). The time-varying passive-tracer concentration serves as one of the pieces of evidence for the upward lift of water particles as well. After 70 days, the penetration of SCC-layer water onto the ECS shelf is evident in the central region (around 26°N to 28°N) and the northern region (around 30°N) of the ECS slope. This pattern aligns with the trajectories observed for the group 2 drifters. The vigorous onshore intrusion northeast of Taiwan Island is accurately captured as well, which shows similar patterns to previous studies (e.g., Yang, Yin, et al., 2018). It is worth mentioning that nearly 60% of the ECS is covered with passive tracers which originates from the SCC layer inside the OT after a 1-year simulation.

The upwelling connected with the onshore intrusion is very obvious. Figures 6a and 6b respectively show the vertical velocity at the 26.6 and 27.3 σ_θ surface. In Figure 6a, the strong upwelling pattern at the 26.6 σ_θ surface is highly consistent with the passive tracer distribution near the ECS slope. In other words, regions with strong

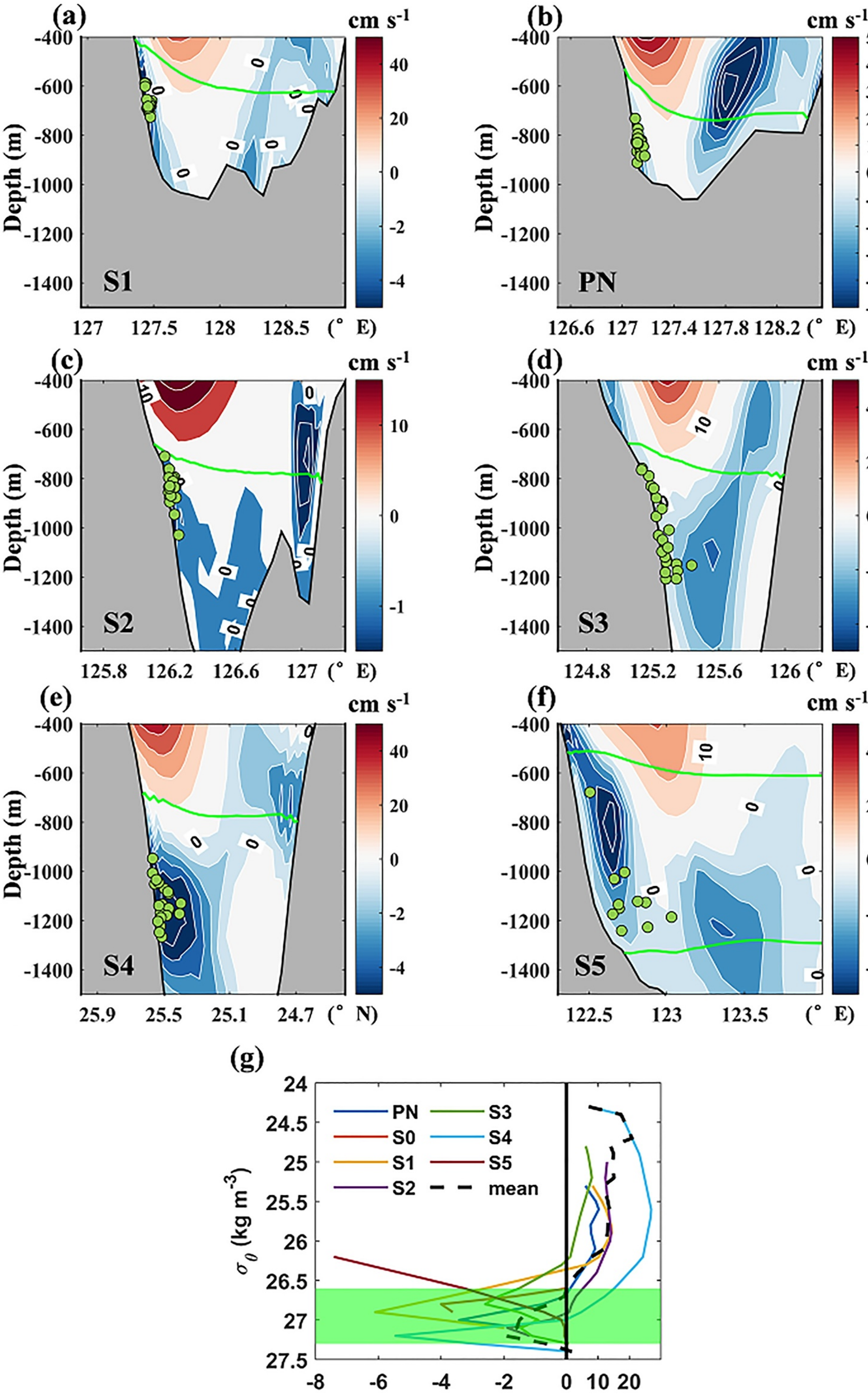

Figure 4. The distribution of SCC in the deep Okinawa Trough. (a–f) The normal velocity at S1, PN, and S2–S5, respectively (northeastward positive). The green lines are respectively the 26.6 and 27.3 σθ surfaces. The green dots depict the location of the drifters when they pass through S1–S5. The contour intervals are different for positive and negative values. (g) The cross-transect velocity over sloping bottom as a function of potential density. The green patch indicates the potential density range for the SCC.

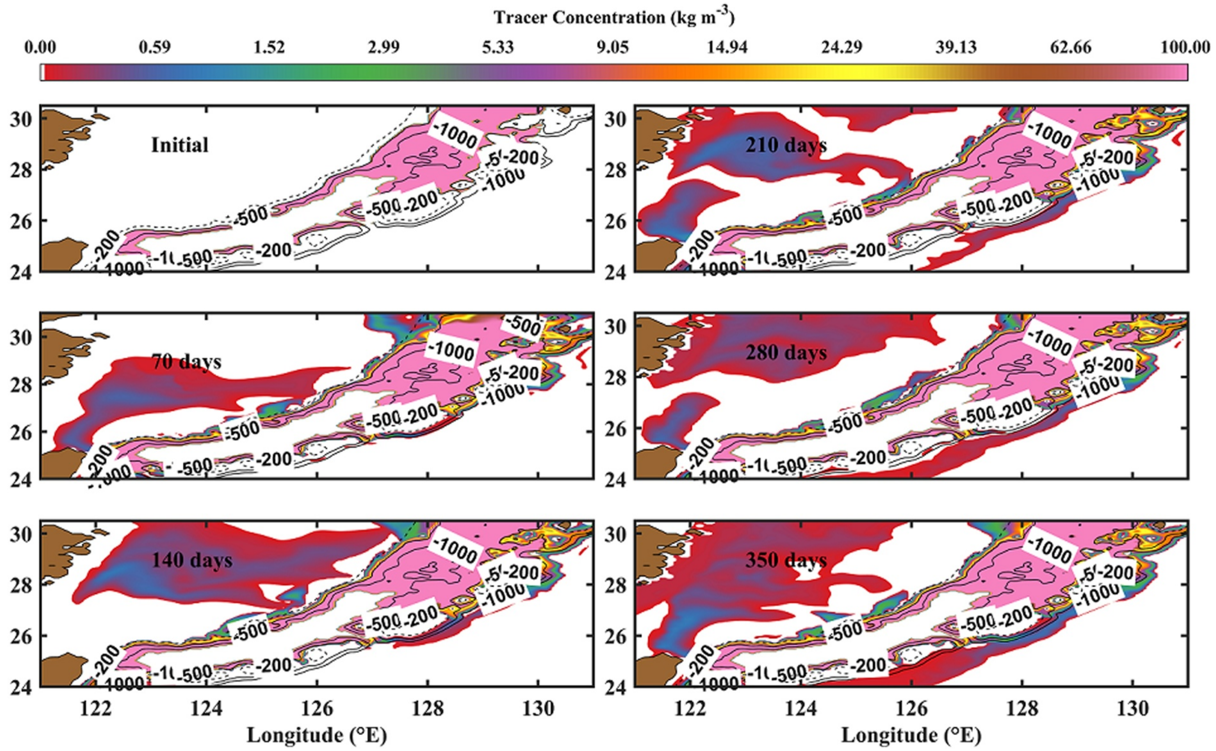

Figure 5. Time-varying tracer concertation at the bottom terrain-following layer for passive tracers. The dashed line represents the 200-m isobaths, while the 500-m and 1000-m isobaths are indicated by solid lines.

background upwelling are generally accompanied by active onshore intrusions of passive tracers. Relative to the vertical motions at the 26.6 σ_θ surface, those at the 27.3 σ_θ surface are much less active. Across the entire OT, the SCC layer experiences an annual loss of 0.52 Sv at the 26.6 σ_θ surface and gains 0.07 Sv at the 27.3 σ_θ surface. This results in a net loss of 0.45 Sv vertically, contributing to a divergent SCC layer. Notably, it is reported by Zhang et al. (2017) that the bottom-layer cross-shelf transport into the ECS shelf in the sloping regions is about 0.7 Sv, which is comparable with the 0.52 Sv in our case. Therefore, ESOM simulation shows that the SCC plays a surprisingly crucial role in shaping the hydrological environment of the ECS.

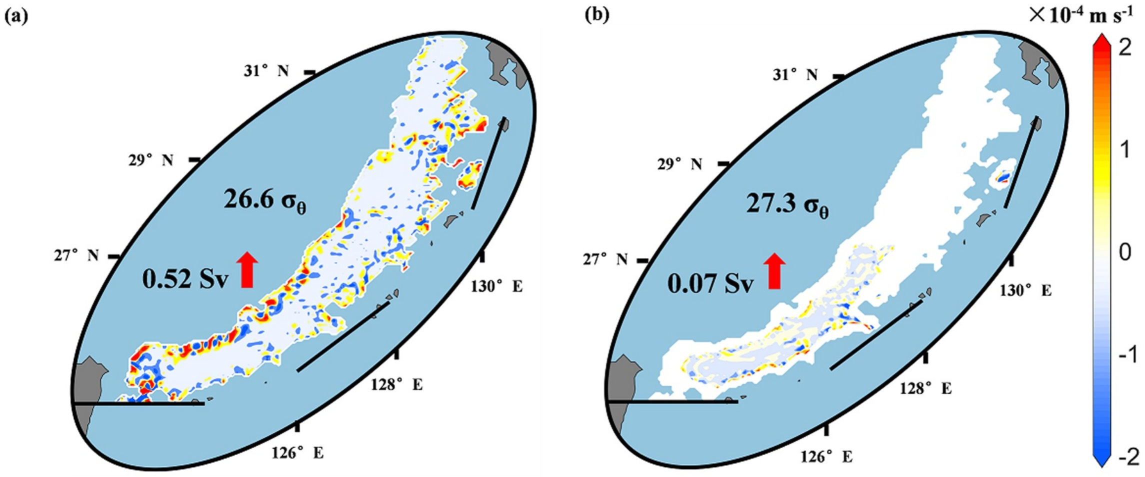

Figure 6. Upwelling divergence in the deep Okinawa Trough. (a) Annually averaged vertical velocity at the 26.6 σ_θ surface. Regions shallower than the depth minimum of the 26.6 σ_θ surface or out of the Okinawa Trough are masked by blue shading. Panel (b) same as pane (a), but for the vertical velocity at the 27.3 σ_θ surface.

3.3. Trough-Scale Flow Pattern

Sloping bottoms differ from wall-like boundaries in that the intersection between isopycnals and the lateral boundary varies horizontally with depth. To better illustrate the deep circulation, especially the SCC near the ECS continental slope, the flow fields near the OT boundary and in the inner OT are calculated separately. The flow pattern over the sloping bottom is computed as follows.

The 26.6 σ_θ surface, serving as the upper boundary of the SCC layer, intersects with the OT slope. These intersections are indicated by the edge of the blue shading in Figure 7a, which signifies the upper edge of the OT slope within the SCC layer.

The centers of the OT slope (indicated by black triangles in Figure 7b) are selected as grid points located three grid points inward from the eastern and western edges, with necessary artificial modifications operated near the openings and eastern OT slope to make the closed line in Figure 7a smooth. When averaging the current velocities around these centers, the algorithm searches for the closest available points at each isopycnal surface within a radius of 5 grid points (the yellow circle in Figure 7b) and then averages them. The purple triangles in Figure 7b are regarded as the inner OT points, and their velocity are vertically averaged (the green and blue arrows in Figure 7a). Note that in regions where the potential density at the sea bottom is less than 27.3, the average current velocity in the SCC layer is calculated by averaging the vertical integration from the 26.6 σ_θ surface to the deepest σ_θ surface available, which is the closest σ_θ surface near the sea bottom.

This averaging method is operated at the model grids but here we use the PN transect as a comprehensive example. Figure 7c shows the vertical slice of potential density at the PN transect in which the original s-coordinate model outputs at each horizontal grid points (density points) are then vertically interpolated onto σ_θ surfaces between 26.6 and 27.3 with a 0.1 kg m^{-3} interval. Note that the 27.2 and 27.3 σ_θ surfaces are absent in Figure 7c due to the limited bathymetry. The dots in Figure 7c are the interpolated locations at the PN transect from the ROMS grid points, and the intersections between the bottom topography and the 27.0 σ_θ surface, as well as the 27.1 σ_θ surface, will not actually be taken into account if this method is conducted here.

Shown in Figure 7a, the SCC, characterized by a maximum speed exceeding 6 cm s^{-1}, exhibits continuity along the deep western boundary. On the eastern side of the OT, the boundary current demonstrates heightened complexity. A relatively weaker current flows northeastward along the western side of the Ryukyu Islands. This northeastward current tends to intensify northeast of Taiwan but weakens as it passes the western side of the Okinawa and Amami Islands. Collaboratively, these details give rise to a potential trough-scale continuous SCC and a cyclonic circulation pattern at the OT boundary. Importantly, a well-defined cyclonic eddy is located in the northern OT region, near S1, contributing to a localized intensification of the SCC. Along the western boundary of the Tokara Islands, the Kuroshio Counter Current (KCC) flows intensively southward at coordinates 129°E, 29.5°N. This strong KCC causes the original SCC, which typically flows northward in this region, to disappear. Additionally, the branch of the Kuroshio flowing northward over the slope of the SSC layer northwest of the Tokara Strait appears to be the source of the SCC that forms the cyclonic circulation at the head of the OT southwest of Kyushu as well.

These findings substantiate our perspective that the SCC represents a spatially continuous flow linked to the potential trough-scale cyclonic circulation accompanied by upwelling in the slope region around the OT. In the subsequent sections, we provide further analysis to show its formation mechanism.

4. Mechanism

In the case of a semi-enclosed deep basin like the OT, the deep circulation is typically linked to lateral volume transport (LVT). The OT undergoes substantial exchanges of deep water with adjacent seas, primarily through three openings, as illustrated in Figure 4a for their locations. Transect 1 (T1) is situated at the East Taiwan Channel (ETC), where the lower envelope of the Kuroshio Current extends to a 1-km depth. Transect 2 (T2) is located at the Kerama Gap, dominated by inflow from the northwest Pacific Ocean. Transect 3 (T3) is positioned at the Tokara Strait, representing the exit spot of the Kuroshio Current from the OT.

Figure 8 illustrates the deep LVT (layer between 26.6 and 27.3 σ_θ surfaces) through these transects (inflow considered positive). The transport into the OT predominantly occurs across T1 and T2, with annual mean values of approximately 0.83 and 0.30 Sv, respectively. The primary outflow transport from the OT takes place through

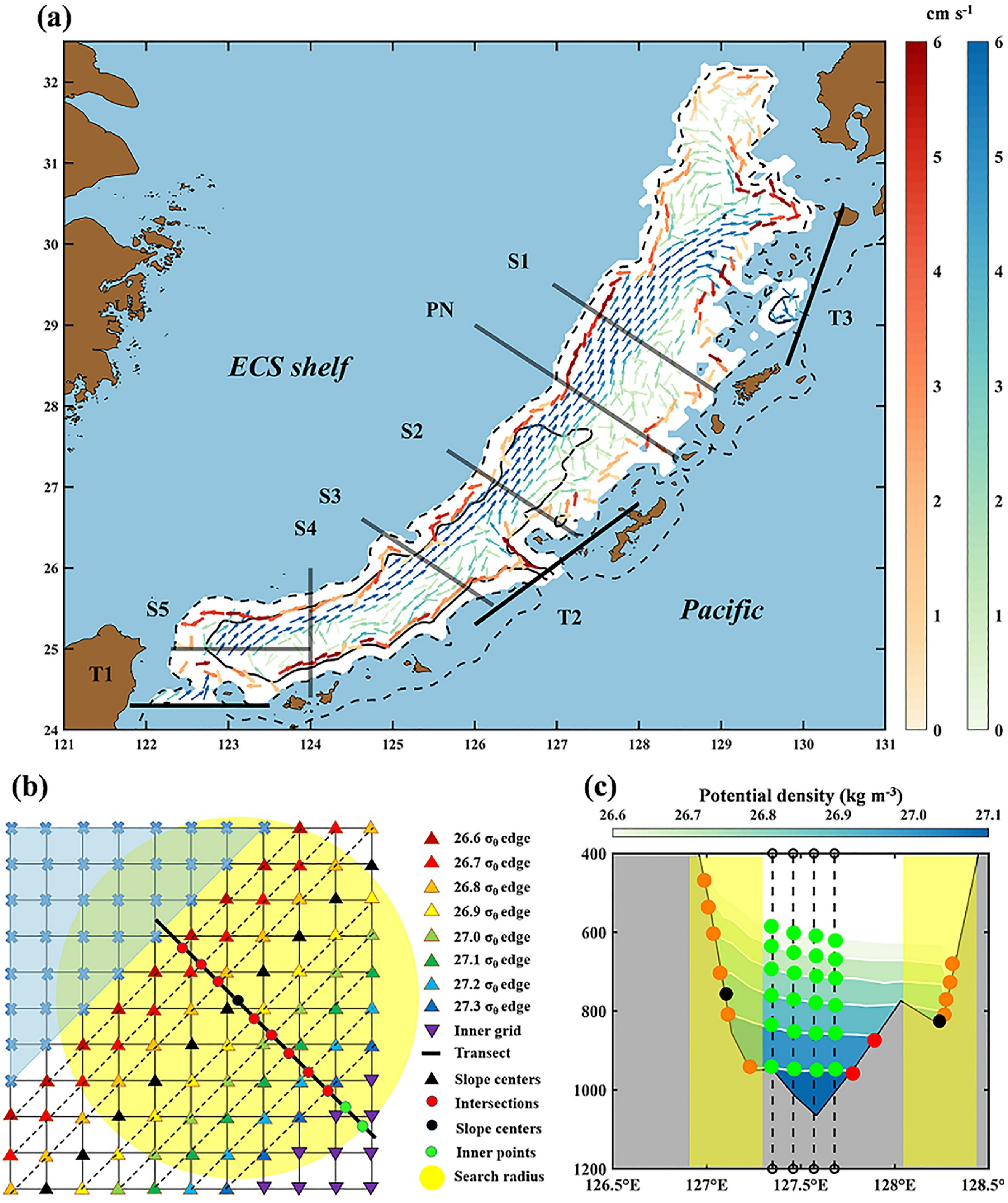
(a)
cm s-1
ECS shelf
Pacific
S1
PN
S2
S3
S4
S5
T1
T2
T3
32
31
30
29
28
27
26
25
24
121
122
123
124
125
126
127
128
129
130
131
6
5
4
3
2
1
0
(b)
26.6 σθ edge
26.7 σθ edge
26.8 σθ edge
26.9 σθ edge
27.0 σθ edge
27.1 σθ edge
27.2 σθ edge
27.3 σθ edge
Inner grid
Transect
Slope centers
Intersections
Slope centers
Inner points
Search radius
(c)
Potential density (kg m-3)
26.6
26.7
26.8
26.9
27.0
27.1
400
600
800
1000
1200
126.5°E
127°E
127.5°E
128°E
128.5°

Figure 7.

T3, accounting for approximately 0.94 Sv annually. The LVT through T1 to T3 advect PV and directly influences the PV budget in the OT. To elucidate the mechanism behind the cyclonic circulation pattern, we employ the PV constraint (Yang, 2005; Yang & Price, 2000, 2007):

$$\underbrace{\frac{\partial}{\partial t}\left(\oint_C\left(\vec{u_h}\cdot\vec{l}\right)dl\right)}_{ACCEL}+\underbrace{\sum_{i=1}^{N}\frac{Q_i f_i}{H_i}}_{LPV}+VPV=VS-\lambda\underbrace{\oint_C\left(\vec{u_h}\cdot\vec{l}\right)dl}_{DISS} \tag{1}$$

In Equation 1, C is a closed circle, $\boldsymbol{l}$ is the unit vector tangential to C, ds is an element length, $\boldsymbol{u_h}$ is the horizontal component of the velocity vector. Term ACCEL is the accelerating term which is usually omitted at a steady state. Term LPV is the net PV transport across C (influx positive), where Q_i, f_i, and H_i are respectively the volume transport, Coriolis parameter, and the layer thickness at the ith opening. Term VPV and VS are respectively the advective vertical PV transport and the vortex stretching term, these two terms are weak below the main thermocline (300 m at most over the ECS slope) and act to cancel each other because they contribute to the total PV oppositely (see Appendix A). VPV and VS are calculated by interpolating the vertical velocity, which shows strong upwelling features near the ECS slope, onto the upper and lower boundaries of the SCC layer, which are the 26.6 and 27.3 σ_θ surfaces, respectively (Figure 6). Due to changes in bottom topography, the 27.3 σ_θ surface covers only the southern OT (Figure 7a). Term DISS is the lateral (bottom) frictional torque (also known as the dissipation term), where λ is the Rayleigh friction coefficient, $\boldsymbol{u_h}$ is the horizontal component of the velocity vector. It has been noted that the PV constraint is mainly a balance between the LPV and DISS term beneath the main thermocline (Yang & Price, 2000; Zhu et al., 2017, 2019), the depth of which is 300 m at most over the ECS slope. It states that the net lateral PV transport into an area bounded by a closed contour C is balanced by the lateral frictional torque. A positive net PV transport, for instance, is balanced by an anti-cyclonic frictional torque, which is often associated with cyclonic circulation along C.

Yang and Price (2000, 2007) conducted a series of idealized numerical experiments using a reduced-gravity model to investigate the influence of the PV constraint on boundary currents. In this study, we employ ESOM simulations to investigate whether the deep cyclonic circulation in the OT, especially the SCC, is linked to lateral PV transport.

The mean velocity along bottom slope signifies the boundary flow within the SCC layer. The DISS term is integrated along the circle outlined by the locations of the red arrows in Figure 9, approximately following the edge of the 26.6 σ_θ surface inside the OT. The Rayleigh friction coefficient λ is typically assigned subjectively. For example, Yang and Price (2000) utilized $\lambda = 1.36 \times 10^{-6}$ s^{-1}. Huang and Yang (1996) directly estimated λ-10^{-6} s^{-1}. Here we apply a rigorous approach to set λ by applying linear regression between the bottom stress and bottom current velocity within the OT. The linear regression coefficient yields $\lambda = 5.17 \times 10^{-6}$ s^{-1}. The contribution of the terms in Equation 1 is shown in Figure 8, it is estimated an annual net lateral PV transport of 0.034 m^2 s^{-2} enters the deep OT and a comparable total PV of 0.029 m^2 s^{-2} is dissipated through bottom friction. The other terms, including VPV, VS, and ACCEL, are two orders of magnitude smaller than the main balanced terms. Specifically, the bars for the latter three terms are enlarged by a hundredfold. Notably, VPV and VS effectively counteract each other, as elucidated in Appendix A. This robust balance here agrees well with those in deep layers of other semi-enclosed basins (Yang & Price, 2000; Zhu et al., 2017, 2019).

Figure 7. (a) Mean currents at the SCC layer (between 26.6 and 27.3 σ_θ surface). The black dashed lines are the 500-m isobaths. Regions shallower than the depth minimum of the 26.6 σ_θ surface or beyond the Okinawa Trough are masked with blue shading. T1–T3 serves as three pathways enabling the exchange of deep water. The PN and S1–S5 transects are cross-shelf transects at the ECS slope. (b) An idealized schematic for the averaging method. The gridded map illustrates the density-points of the horizontal Arakawa-C grid over a sloping bottom, where the bathymetry deepens southeastward, resembling the East China Sea continental slope. Blue crossings denote the density points where bottom density is smaller than 26.6 σ_θ, and these points are masked by blue shading. The triangles mark the density grid points. Black triangles represent the slope centers, purple triangles denote the inner grid points outside the sloping bottom, and other colored triangles depicts the densest σ_θ at each location, with dashed lines connecting them to show the edges of these isopycnal levels. Note that these triangles may exhibit irregular distribution and coincide with each other due to the limited resolution in model simulations. The black solid line denotes an example of a cross-shelf transect, with the black dot representing the interpolated slope center, and red dots indicating the corresponding intersections between the slope and different isopycnals. The yellow circle shows the search radius used during averaging. (c) Potential density stratification of SCC layer at PN transect. The black dots are the centers of the slopes. The red dots signify the intersections between isopycnal layers from 26.6 to 27.3 σ_θ with 0.1 interval and the ocean bottom within the sloping region, as shown by the yellow rectangles. The green dots represent the standard isopycnal layers within the Okinawa Trough.

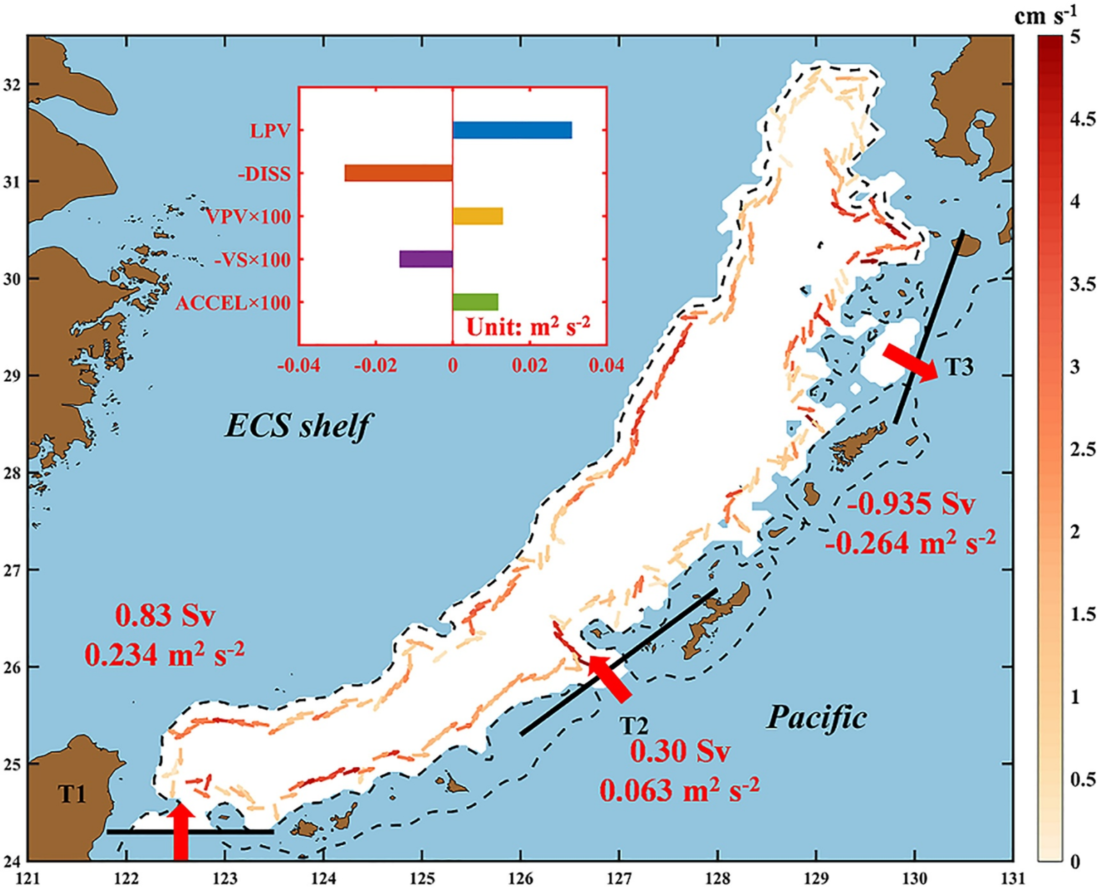

Figure 8. Potential vorticity balance in the deep Okinawa Trough (between 26.6 and 27.3 σ_θ surface). The arrows show the vertically averaged boundary current velocity, their locations show the closed line along which the line integral is conducted. The black dashed line shows the 500-m isobath. Note that the terms VPV, VS, and ACCEL are enlarged by a hundredfold.

The balance between the LPV and DISS could potentially be a coincidence since there are a lot of differences between an idealized model framework and ROMS. It is important to validate such balance through sensitivity experiments. Designing numerical experiments to verify the PV constraint with primitive-equation models is challenging, especially in an irregularly shaped basin like the OT. It is tempting but impractical to freely manipulate the lateral PV input into the OT and observe the corresponding response in the deep circulation. Modifying transports at the model boundary is a straightforward task, but it typically has minimal impact on the interior of the model. On the other hand, it is even less feasible to directly alter the fluxes at T1-T3. However, the following approach makes an exception and resolves this dilemma by leveraging the unique characteristics of the western boundary current region in the North Pacific Ocean.

Circulations over 2,000 m depth in the western boundary current region in the North Pacific Ocean are significantly influenced by large-scale forcings, such as the wind stress curl and its associated signals. These factors are encompassed in the open boundary conditions of regional models like ESOM. In essence, the western boundary current region in the North Pacific Ocean serves as the recipient of open boundary messages, and changes in the open boundary conditions will definitely affect circulation features in the OT. The inflow and outflow into the OT exhibits significant seasonal contrast between July and January because of the ECS-Kuroshio intensity difference as reported by previous studies (Guo et al., 2003, 2006; Hu et al., 2020; Yang, Huang, et al., 2018). Therefore, the disparity in open boundary conditions between January and July may partly contribute to the change in the mean-state deep circulation. To validate this deduction, we conducted two additional cases by modifying the open boundary conditions (see Figure 1 for boundary locations). Case BRY07 and case BRY01 are run under fixed open boundary conditions in July and January from the coarse model in all 12 months to simulate scenarios with different net PV transport into the OT.

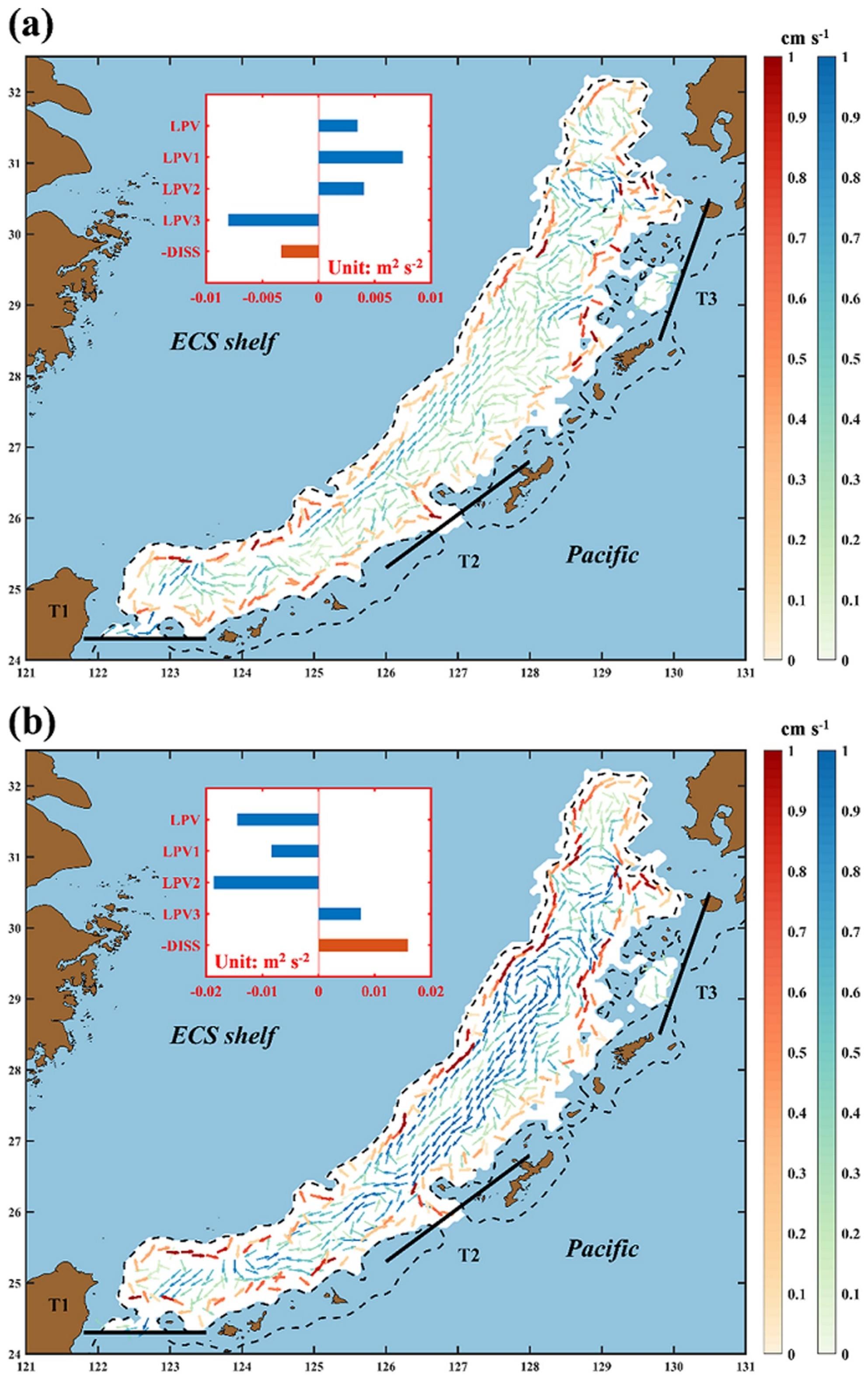

Figure 9. The sensitivity of PV constraint in the Okinawa Trough. (a) The difference between case BRY07 and Control. The arrows denote the velocity anomaly (red for the boundary and green for the inner trough) panel (b) same as pane (a), but for the difference between BRY01 and Control run.

Compared with the Control run, when the deep OT experiences a positive (negative) anomaly of PV influx, as evident in cases BRY07 (BRY01), a cyclonic (anticyclonic) circulation anomaly emerges along the OT boundary (refer to Figures 9a and 9b). This consensus is quantitively illustrated in the bar plots, in which the LPV term increases by 11% in BRY07, while in BRY01, the LPV term decreases by 48%. The DISS term exhibits comparable changes correspondingly, indicating the balance between them still holds, and the deep circulation adjusts to the LPV change through bottom dissipation. Therefore, the robustness of the PV constraint is verified by these experiments.

Although the validity of PV constraint in the deep OT is demonstrated, it is yet not clear why the net PV influx is always positive and induces a cyclonic circulation pattern. In the following, we address that the divergence of upwelling, which mostly results from the onshore intrusion of the deep water, is the driving factor for the potential trough-scale cyclonic circulation.

The vertical displacements of water particles lead to upwelling divergence in the SCC layer (illustrated in the previous section), necessitating LVT to compensate. In an annual mean state, the loss of water volume is expected to be compensated by LVT through T1-T4 since ROMS conserves volume. ESOM anticipates that there is a net LVT of 0.45 Sv annually in the SCC layer of OT. Although the net LVT is not a perfect match for the loss of volume from the upwelling divergence, this result is totally understandable considering the uncertainty in interpolation.

Assuming the water through the openings conserves volume and advects constant PV f_0/H_0, Equation 1 can be reformulated through the divergence theorem as (see Appendix A):

$$(W_1 - W_2)\,\frac{f_0}{H_0} = -\lambda \oint_C (\boldsymbol{u_h} \cdot \boldsymbol{l})\, dl \tag{2}$$

where W_1 and W_2 are respectively the area integrated vertical volume transport at the upper layer and lower layer (26.6 and 27.3 σ_θ surface in this case) in the OT, f_0/H_0 denotes the constant PV. Equation 2 means upwelling divergence accompanied with horizontal outflow from the inner area to surrounding shelf slope area induces positive LVT, which transports PV and hence results in the cyclonic circulation.

Subsequently, two experiments (case ANSOURCE and case ANSINK) are additionally conducted to show that the upwelling divergence indeed manipulates the boundary circulation in the SCC layer. In the case of ANSOURCE (ANSINK), a total amount of 0.5 Sv point source (sink) is introduced along the ECS slope between 26.6 and 27.3 σ_θ surface to alter the upwelling divergence in the SCC layer. As anticipated, Figure 10a (10b) illustrates a notable anticyclonic (cyclonic) circulation anomaly in the southern OT, accompanied by reduced (increased) LVT through the openings. The changes in LVT in ANSOURCE and ANSINK are most significant through the Kerama Gap, indicating the unique importance of this deep channel in regulating the deep circulation in the OT. In Figure 10a, these noteworthy velocity anomalies are primarily concentrated in the vicinity of the applied source (sink) regions. This can be explained as follows: the LVT acts to offset the effects of the extra sources and sinks, causing alterations in local PV. As a result, bottom friction responds by adjusting the boundary flow to eliminate these changes.

Based on the analyses above, we conclude that the upwelling divergence in the OT is the driving factor for the potential trough-scale SCC over the ECS continental slope.

5. Discussions

It is noteworthy that the circulation pattern depicted in Figure 10a deviates from the typical spatial distribution of SCC intensity. This diversity is marked by a notable contrast in SCC intensity particularly in the northern OT, where SCC maintains relatively strong intensity despite the comparatively weak upwelling in the northern ECS slope. This suggests that while the upwelling divergence in the ECS slope plays an essential role in driving a trough-scale cyclonic circulation pattern in Figure 10a, there are other processes at play that locally intensify the SCC. For example, Nakamura (2005) and Nakamura et al. (2008, 2021) have addressed the existence of the SCC at the northern OT which results from the baroclinic instability of the surface Kuroshio front. Our experiments suggest that the seasonality of the open boundary conditions in the NEST2 model seems to give rise to an eddy-like flow pattern in the northern OT (figure not shown), which provides evidence for Nakamura's conclusion

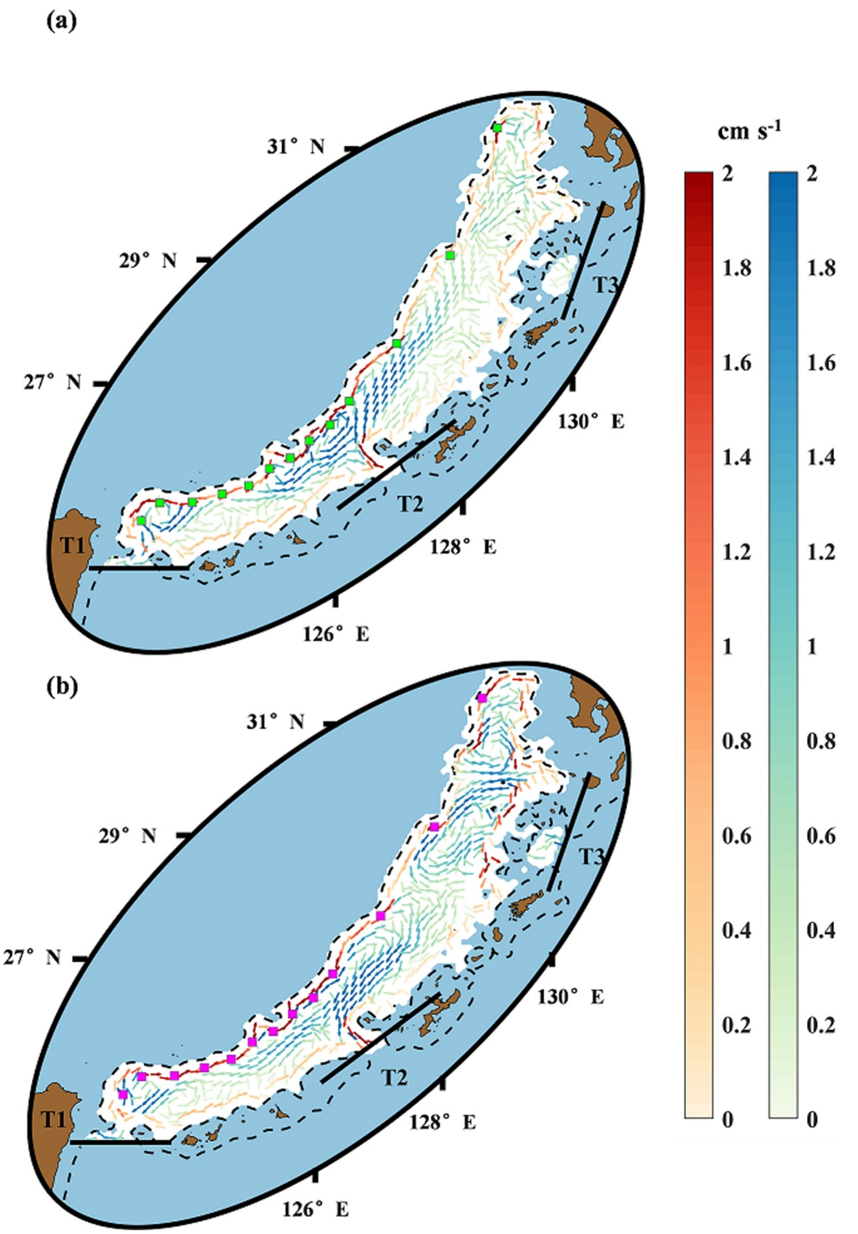

Figure 10. Circulation anomalies from source and sink experiments. (a) The difference between case ANSINK and the Control run. (b) The difference between case ANSOURCE and the Control run. The green rectangles denote point sources of water volume, while the red ones represent the opposite.

because baroclinic instability is stronger when the Kuroshio path meander tends to be less stable with seasonal open boundary conditions.

Upwelling and onshore intrusion are quite common and often occur together over the ECS continental slope. Various mechanisms have been proposed to explain this phenomenon in distinct regions, each involving unique processes. One of the dominant processes is the generation of frontal eddies from the Kuroshio front. It is reported that the central region of the Kuroshio frontal eddy is characterized by the upwelling of slope water (Qiu et al., 1990; Sugimoto et al., 1988) and considerable amount of slope water is transport to shallower regions of the ECS shelf (Isobe & Beardsley, 2006). In the real ocean, each of these eddies is unique and nearly impossible to be reproduced through climatological simulations like ESOM. However, the significant period band around 10–20 days in the power spectrum in Figure 2c suggests that ESOM partially captures their influence on the mean-

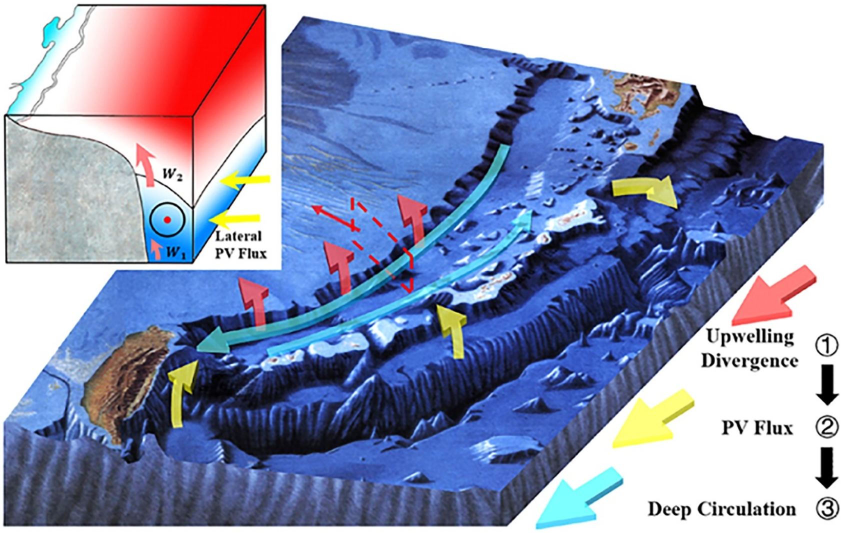

Figure 11. Schematic of the formation mechanism of the slope countercurrent over the East China Sea continental slope.

state upwelling pattern. It has also been addressed that the vigorous Kuroshio Current meeting with the zonal-running steep topography northeast of the Taiwan Island induces the local upwelling, serving as one the important source of the onshore intrusion into the ECS shelf (Yang, Huang, et al., 2018). Strong upwelling is evident in the region southwest of Kyushu as well, where divergence occurs as the Kuroshio Current moves away from the continental slope (Lie et al., 1998). Other processes, including non-uniform heat flux (Oey et al., 2010), the joint effect of baroclinicity and relief (Guo et al., 2003, 2006), and shear stress (Wei, 2018), collectively contribute to the annual-mean upwelling pattern. Consistent with previous studies, this paper confirms that the SCC layer experiences water loss due to upwelling, with lateral volume transport serving as a compensation.

The SCC over the ECS continental slope is in a sense boundary flow that counters the surface Kuroshio. From a trough-scale perspective, this continuous countercurrent may potentially have a profound influence on mass, heat, and nutrient transport. The Kuroshio onshore intrusion northeast of Taiwan Island has been extensively investigated in the past decade. There is a near consensus that the surface Kuroshio water and the Kuroshio subsurface water are the main sources of the intruded water. However, this study brings new insight into this vigorous intrusion event in that the SCC over the ECS continental slope also contributes to the penetration. More details on the mass transport of the SCC will be presented in future studies.

The OT is known as an active place for hydrothermal vents and cold seeps which transfer and exchange materials and energies. As the SCC is positioned directly over the ECS continental slope and exhibits bottom intensification near the locations of the hydrothermal vents and cold seeps, it is highly probable that sediment distribution OT is profoundly influenced by it. When connected with the active upwelling near the ECS slope, the SCC may also play a vital role in maintaining regional biodiversity, and the ESOM simulation above serves as supporting evidence.

In this study, we demonstrate the mechanism for the SCC using a numerical model and physical interpretations. Understanding the SCC is greatly beneficial for identifying its role in the regional climate, geology, and ecosystem. The dynamical process we illustrate in Figure 11 may potentially be universal in any other western boundary current regions with sloping bottoms because the bottom stress, which determines the bottom Ekman transport, is large and varies significantly with depth in sloping bottoms. The convergence and divergence of bottom Ekman transport in the sloping region may induce LVT which advect PV and drive the sense boundary flow.

The variabilities of the SCC on various timescales are widely reported while still require in-depth understanding. Hence, to fill in the missing pieces of this puzzle, additional observations and studies are required to quantify the spatial and temporal variations in the SCC, particularly on the key period band where the eddy effect might be dominant. Future research should also place greater emphasis on investigating the variability of the SCC and its connection to the surface Kuroshio, which is beyond the scope of this study.

6. Conclusions

We focus on the SCCs reported by historical observations at different sites over the ECS continental slope. The SCCs have long been regarded as parts of the cyclonic eddies in the northern OT. Our study reveals that SCC is associated with OT-wide cyclonic circulation, and it is potentially continuous over the ECS continental slope. The trough-scale circulation in the lower-layer OT is primarily driven by upwelling divergence. In the sloping region, the divergence of upwelling induces LVT that advects PV mainly through three transects. In annual mean climatology, volume transport of 0.83 and 0.30 Sv enter the OT through the passage over the ETC and the Kerama Gap respectively. A lower-layer volume transport of 0.94 Sv leaves the OT through the Tokara Strait. These three fluxes together result in a positive net PV transport of 0.034 $\mathrm{m}^2\ \mathrm{s}^{-2}$ into the lower-layer OT, which requires negative frictional torque to balance it, and therefore a trough-scale cyclonic circulation exits along the OT boundary. This process is illustrated by a schematic in Figure 11. This circulation pattern is clearly depicted in the well-validated ESOM simulations. The SCC is weak but stable with a mean magnitude of $O(1)$ cm s^{-1}, which is much weaker compared to the Kuroshio Current that lies over it. It is also found that not only the Kuroshio Current but also the SCC substantially contributes to the onshore intrusion, providing a new perspective for comprehending the intricate circulation patterns in the northwest Pacific Ocean.

Appendix A: Derivation of PV Constraint

The following derivation is most similar to that in Yang and Price (2000), except that we keep additional terms that might potentially contribute to the PV balance. In a deep basin filled with incompressible and stratified seawater (Pedlosky, 1979; Rhines, 1983; Yang & Price, 2000), the vorticity equation can be written as:

$$\frac{D}{Dt}\left(\nabla\times\vec{u}+2\vec{\Omega}\right)=\left(\left(\nabla\times\vec{u}+2\vec{\Omega}\right)\cdot\nabla\right)\vec{u}-\lambda\nabla\times\vec{u} \tag{A1}$$

where $\vec{u}=(u,v,w)$ is the vector of velocity, $\vec{\Omega}$ is the vector of Earth's rotation, and λ is the Rayleigh friction coefficient.

The vertical component of the vorticity yields:

$$\frac{\partial\zeta}{\partial t}+\vec{u}\cdot\nabla(f+\zeta)\ =\ (f+\zeta)\frac{\partial w}{\partial z}-\lambda\zeta \tag{A2}$$

where f is the Coriolis parameter, and $\zeta = \partial v/\partial x\text{-}\partial u/\partial y$ is the relative vorticity. Applying the non-divergence condition which means $\nabla\cdot\vec{u}=0$, the Equation A2 becomes

$$\frac{\partial\zeta}{\partial t}+\nabla\cdot\left[\vec{u}(f+\zeta)\right]\ =\ (f+\zeta)\frac{\partial w}{\partial z}-\lambda\zeta \tag{A3}$$

Separating the divergence term on the left-hand side into the horizontal and vertical components, Equation A3 can be written as

$$\frac{\partial\zeta}{\partial t}+\nabla_h\cdot\left[\vec{u_h}(f+\zeta)\right]+\underbrace{\frac{\partial}{\partial z}(w(f+\zeta))}_{T_1}=\underbrace{(f+\zeta)\frac{\partial w}{\partial z}}_{T_2}-\lambda\zeta \tag{A4}$$

where $\vec{u_h}=(u,v)$ denotes the horizontal velocity vector, $\nabla_h\cdot=\partial/\partial x+\partial/\partial y$ is the horizontal divergence operator.

The term T_1 and T_2 looks similar to each other but they signify distinct processes. T_1 means the vorticity transport by the vertical volume transport, while T_2 denotes the vorticity production from vortex stretching. These two terms cancel because f is independent of z, and ζ is at least one order of magnitude smaller than f in SCC regions

(SCC itself is weak, and hence its relative vorticity, $\zeta\text{-}O(10^{-6})s^{-1}$. The fact that T_1 and T_2 cancel each other has unique physical meaning. Suppose upwelling is advecting water volume out of a certain layer, it takes planetary vorticity out of this layer, but it also stretches the water column of this layer, so that positive vorticity is produced locally. This locally produced positive vorticity compensates for the loss of planetary vorticity advected by upwelling.

The analysis above indicates that the vertical velocity w does not directly contribute to the vorticity budget. However, most versions of the PV budget equation (also derived from the vorticity budget) fail to reveal this process and thus tend to relatively overestimate the vorticity (or PV) contribution from w (Yang & Price, 2000). This is due to the quasi-geostrophic (QG) approximation during their derivations. In the QG framework, w vanishes to the lowest order, which kills the role of w in vertically advecting momentum and vorticity. Pedlosky (1996) has addressed this issue (see his page 99) and provides the QG vorticity (see his equation 3.2.11) as

$$\frac{\partial\zeta}{\partial t}+\nabla_h\cdot\left[\overrightarrow{u_h}(f+\zeta)\right]=\underbrace{(f+\zeta)\frac{\partial w}{\partial z}}_{T_2}-\lambda\zeta \tag{A5}$$

As a consequence, the counterpart of vorticity (or PV) contribution of w (T_2, the vortex stretching from the continuity of mass), however, is left in QG equations. In this regard, it is better to keep both T_1 and T_2 so that their effects can cancel each other as is supposed to be.

Given that f is independent of z, we can express these two terms as

$$T_1=f\partial w/\partial z+\partial(w\zeta)/\partial z \tag{A6}$$

and

$$T_2=f\partial w/\partial z+\zeta\partial w/\partial z. \tag{A7}$$

Since both T_1 and T_2 involve term $f\partial w/\partial z$, they can be further simplified as

$$T_{1r}=\partial(w\zeta)/\partial z \tag{A8}$$

and

$$T_{2r}=\zeta\partial w/\partial z, \tag{A9}$$

where the subscript 1r and 2r respectively mean the relative vorticity contribution on T_1 and T_2. To include as much information as possible, we still keep the distinguished terms T_{1r} and T_{2r} during the derivation. Following Equation A4, we conduct a vertical integration from $D_1(x, y)$ to $[D_1+D(x, y)]$, where $D(x, y)$ is the temporal average thickness of a certain isopycnal layer, we have

$$\begin{aligned}&\frac{\partial}{\partial t}\left[\int_{D_1}^{D_1+D}\left(\frac{\zeta}{D}\right)dz\right]+\nabla_h\cdot\int_{D_1}^{D_1+D}\left[\overrightarrow{u_h}\left(\frac{f+\zeta}{D}\right)\right]dz+\int_{D_1}^{D_1+D}\left[\frac{1}{D}\left(\frac{\partial w\zeta}{\partial z}\right)\right]dz\\&=\int_{D_1}^{D_1+D}\left[\frac{\zeta}{D}\left(\frac{\partial w}{\partial z}\right)\right]dz-\lambda\int_{D_1}^{D_1+D}\left(\frac{\zeta}{D}\right)dz\end{aligned} \tag{A10}$$

and can be simplified as

$$\frac{\partial\overline{\zeta}}{\partial t}+\nabla_h\cdot\left[\overrightarrow{U_h}\left(\frac{f+\overline{\zeta}}{D}\right)\right]+\frac{1}{D}\left(w\zeta|_{D_1+D}-w\zeta|_{D_1}\right)=\int_{D_1}^{D_1+D}\left[\frac{\zeta}{D}\left(\frac{\partial w}{\partial z}\right)\right]dz-\lambda\overline{\zeta} \tag{A11}$$

where $\overrightarrow{U_h}$ is the depth-integrated velocity, $\overline{\zeta}$ is the vertical mean ζ, and $(f + \zeta)/D$ is PV. Upon conducting an integration over the whole basin S,

$$\begin{aligned}&\iint_S \frac{\partial \overline{\zeta}}{\partial t} dx\,dy + \iint_S \nabla_h \cdot \left[\overrightarrow{U_h}\left(\frac{f+\overline{\zeta}}{D+h}\right)\right] dx\,dy + \iint_S \frac{1}{D}\left(w\zeta|_{D_1+D} - w\zeta|_{D_1}\right) dx\,dy \\ &= \iiint_V \left[\frac{\zeta}{D}\left(\frac{\partial w}{\partial z}\right)\right] dx\,dy\,dz - \iint_S \lambda \overline{\zeta} dx\,dy \end{aligned} \tag{A12}$$

Applying the divergence theorem and Stokes theorem, Equation A12 is transformed to

$$\begin{aligned}&\frac{\partial}{\partial t}\left(\oint_C \left(\overrightarrow{u_h} \cdot \overrightarrow{l}\right) dl\right) + \oint_C \left(\overrightarrow{U_h} \cdot \overrightarrow{n}\right)\left(\frac{f+\overline{\zeta}}{D}\right) dl + \iint_S \frac{1}{D}\left(w\zeta|_{D_1+D} - w\zeta|_{D_1}\right) ds \\ &= \iiint_V \left[\frac{\zeta}{D}\left(\frac{\partial w}{\partial z}\right)\right] dv - \lambda \oint_C \left(\overrightarrow{u_h} \cdot \overrightarrow{l}\right) dl \end{aligned} \tag{A13}$$

Considering a deep basin with N openings and $f \gg \zeta$, Equation A13 degenerates into

$$\underbrace{\frac{\partial}{\partial t}\left(\oint_C \left(\overrightarrow{U_h} \cdot \overrightarrow{l}\right) dl\right)}_{Accel} + \underbrace{\sum_{i=1}^{N} \frac{Q_i f_i}{H_i}}_{LPV} + \underbrace{\iint_S \frac{1}{D}\left(w\zeta|_{D_1+D} - w\zeta|_{D_1}\right) ds}_{VPV} = \underbrace{\iiint_V \left[\frac{\zeta}{D}\left(\frac{\partial w}{\partial z}\right)\right] dv}_{VS} \underbrace{-\lambda \oint_C \left(\overrightarrow{u_h} \cdot \overrightarrow{l}\right) dl}_{DISS} \tag{A14}$$

where the term *Accel* is the accelerating term, the term *LPV* is the net lateral PV influx, the term *VPV* is the net vertical PV transport, the term *VS* is the vertical stretching term, and the term *DISS* is the dissipation term.

Equation A14 is the detailed version of Equation 1. In a steady state, with VS and VPV canceling each other, Equation 2 can be easily derived from equation 1 by applying the equation of continuity.

Data Availability Statement

The data used to reproduce the results of this paper are available at https://doi.org/10.6084/m9.figshare.24602691 (Cui & Yang, 2024).

Acknowledgments

This study was supported by the National Natural Science Foundation of China (Nos. 42076022, 92158202 and 42306009), the Strategic Priority Research Program of the Chinese Academy of Sciences (Nos. XDB42000000 and XDA19060203), the National Key Research and Development Plan Sino-Australian Center for Healthy Coasts (No. 2016YFE0101500) and the CAS-CSIRO BAU project (No. 133137KYSB20180141). It was also supported by the High Performance Computing Center at the IOCAS, East China Sea ocean observation and research station of OMORN, and the Youth Innovation Promotion Association CAS. Arthur J. Miller was partly supported by the National Science Foundation (OCE-2022868). Thanks for the data service provided by the Oceanographic Data Center, Chinese Academy of Sciences (CASODC) (http://msdc.qdio.ac.cn). We greatly appreciate the detailed and constructive comments by the two anonymous referees who significantly improved the clarity of this manuscript.

References

Andres, M., Jan, S., Sanford, T., Mensah, V., Centurioni, L., & Book, J. (2015). Mean structure and variability of the Kuroshio from northeastern Taiwan to southwestern Japan. *Oceanography*, *28*(4), 84–95. https://doi.org/10.5670/oceanog.2015.84

Andres, M., Wimbush, M., Park, J. H., Chang, K. I., Lim, B. H., Watts, D. R., et al. (2008). Observations of Kuroshio flow variations in the East China Sea. *Journal of Geophysical Research*, *113*(C5), C05013. https://doi.org/10.1029/2007JC004200

Beal, L. M., & Bryden, H. L. (1997). Observations of an Agulhas undercurrent. *Deep Sea Research Part I: Oceanographic Research Papers*, *44*(9–10), 1715–1724. https://doi.org/10.1016/S0967-0637(97)00033-2

Beckmann, A., & Haidvogel, D. B. (1993). Numerical simulation of flow around a tall isolated seamount, 1, Problem formulation and model accuracy. *Journal of Physical Oceanography*, *23*(8), 1736–1753. https://doi.org/10.1175/1520-0485(1993)023<1736:NSOFAA>2.0.CO;2

Cui, X., & Yang, D. (2024). ROMS simulation on the slope countercurrent over the East China Sea continental slope [Dataset]. *Figshare*. https://doi.org/10.6084/m9.figshare.24602691

Cui, X., Yang, D., Sun, C., Feng, X., Gao, G., Xu, L., & Yin, B. (2021). New insight into the onshore intrusion of the Kuroshio into the East China Sea. *Journal of Geophysical Research: Oceans*, *126*(2), e2020JC016248. https://doi.org/10.1029/2020JC016248

Dee, D. P., Uppala, S. M., Simmons, A. J., Berrisford, P., Poli, P., Kobayashi, S., et al. (2011). The ERA-interim reanalysis: Configuration and performance of the data assimilation system. *Quarterly Journal of the Royal Meteorological Society*, *137*(656), 553–597. https://doi.org/10.1002/Qj.828

Diaz, H., Folland, C., Manabe, T., Parker, D., Reynolds, R., & Woodruff, S. (2002). Workshop on advances in the use of historical marine climate data. *Bulletin of the World Meteorological Organization*, *51*, 377–380.

Dinniman, M. S., Klinck, J. M., & Smith, W. O. (2003). Cross-shelf exchange in a model of the Ross Sea circulation and biogeochemistry. *Deep Sea Research Part II: Topical Studies in Oceanography*, *50*(22–26), 3103–3120. https://doi.org/10.1016/j.dsr2.2003.07.011

Egbert, G. D., & Erofeeva, S. Y. (2002). Efficient inverse modeling of Barotropic Ocean tides. *Journal of Atmospheric and Oceanic Technology*, *19*(2), 183–204. https://doi.org/10.1175/1520-0426(2002)019<0183:Eimobo>2.0.Co;2

Gan, J. P., Liu, Z. Q., & Liang, L. L. (2016). A three-layer alternating spinning circulation in the South China Sea. *Journal of Physical Oceanography*, *46*(8), 2309–2315. https://doi.org/10.1175/JPO-D-16-0044.1

Guo, X., Miyazawa, Y., & Yamagata, T. (2006). The Kuroshio onshore intrusion along the shelf break of the East China Sea: The origin of the Tsushima Warm current. *Journal of Physical Oceanography*, *36*(12), 2205–2231. https://doi.org/10.1175/jpo2976.1

Guo, X. Y., Hukuda, H., Miyazawa, Y., & Yamagata, T. (2003). A triply nested ocean model for simulating the Kuroshio - Roles of horizontal resolution on JEBAR. *Journal of Physical Oceanography*, *33*(1), 146–169. https://doi.org/10.1175/1520-0485(2003)033<0146:Atnomf>2.0.Co;2

Haney, R. L. (1991). On the pressure gradient force over steep topography in sigma coordinate ocean models. *Journal of Physical Oceanography*, *21*(4), 610–618. https://doi.org/10.1175/1520-0485(1991)021<0610:OTPGFO>2.0.CO;2

Hu, F., Liu, Y., Xu, Z., Yin, Y., & Hou, Y. (2020). Bidirectional volume exchange between Kuroshio and East China Sea shelf water based on a whole-region passive-tracing method. *Journal of Geophysical Research: Oceans*, *125*(5), e2019JC015528. https://doi.org/10.1029/2019JC015528

Huang, R. X., & Yang, J. (1996). Deep-water upwelling in the frictional western boundary layer. *Journal of Physical Oceanography*, *26*(10), 2243–2250. https://doi.org/10.1175/1520-0485(1996)026<2243:DWUITF>2.0.CO;2

Ichikawa, H., & Beardsley, R. C. (1993). Temporal and spatial variability of volume transport of the Kuroshio in the East China Sea. *Deep-Sea Research*, *40*(3), 583–605. https://doi.org/10.1016/0967-0637(93)90147-U

Isobe, A., & Beardsley, R. C. (2006). An estimate of the cross-frontal transport at the shelf break of the East China Sea with the finite volume coastal ocean model. *Journal of Geophysical Research*, *111*(C3), C03012. https://doi.org/10.1029/2005JC003290

James, C., Wimbush, M., & Ichikawa, H. (1999). Kuroshio meanders in the East China Sea. *Journal of Physical Oceanography*, *29*(2), 259–272. https://doi.org/10.1175/1520-0485(1999)029<0259:KMITEC>2.0.CO;2

Karcher, M., Kauker, F., Gerdes, R., Hunke, E., & Zhang, J. (2007). On the dynamics of Atlantic water circulation in the Arctic Ocean. *Journal of Geophysical Research*, *112*(C4), C04S02. https://doi.org/10.1029/2006JC003630

Lan, J., Zhang, N., & Wang, Y. (2013). On the dynamics of the South China Sea deep circulation. *Journal of Geophysical Research: Oceans*, *118*(3), 1206–1210. https://doi.org/10.1002/jgrc.20104

Lie, H.-J., Cho, C.-H., & Kaneko, A. (1998). *On the branching of the Kuroshio and the formation of slope countercurrent in the East China Sea, paper presented at Japan-China joint symposium on cooperative study of subtropical circulation system*. Seikai National Fisheries Research Institute, Naha, Japan.

Marchesiello, P., McWilliams, J. C., & Shchepetkin, A. (2003). Equilibrium structure and dynamics of the California current system. *Journal of Physical Oceanography*, *33*(4), 753–783. https://doi.org/10.1175/1520-0485(2003)33<753:ESADOT>2.0.CO;2

Nakamura, H. (2005). Numerical study on the Kuroshio path states in the northern Okinawa Trough of the East China Sea. *Journal of Geophysical Research*, *110*(C4), C04003. https://doi.org/10.1029/2004JC002656

Nakamura, H., Ichikawa, H., Nishina, A., & Lie, H. (2003). Kuroshio path meander between the continental slope and the Tokara Strait in the East China Sea. *Journal of Geophysical Research*, *108*(C11), 3360. https://doi.org/10.1029/2002JC001450

Nakamura, H., Inoue, R., Nishina, A., & Nakano, T. (2021). Seasonal variations in salinity of the North Pacific intermediate water and vertical mixing intensity over the Okinawa Trough. *Journal of Oceanography*, *77*(2), 199–213. https://doi.org/10.1007/s10872-020-00585-z

Nakamura, H., Nishina, A., Ichikawa, H., Nonaka, M., & Sasaki, H. (2008). Deep countercurrent beneath the Kuroshio in the Okinawa Trough. *Journal of Geophysical Research*, *113*(C6), C06030. https://doi.org/10.1029/2007JC004574

Nakamura, H., Nishina, A., Liu, Z., Tanaka, F., Wimbush, M., & Park, J.-H. (2013). Intermediate and deep water formation in the Okinawa trough. *Journal of Geophysical Research OceansOceans*, *118*(12), 6881–6893. https://doi.org/10.1002/2013JC009326

Nishina, A., Nakamura, H., Park, J.-H., Hasegawa, D., Tanaka, Y., Seo, S., & Hibiya, T. (2016). Deep ventilation in the Okinawa Trough induced by Kerama Gap overflow. *Journal of Geophysical Research: Oceans*, *121*(8), 6092–6102. https://doi.org/10.1002/2016JC011822

Oey, L. Y., Hsin, Y. C., & Wu, C. R. (2010). Why does the Kuroshio northeast of Taiwan shift shelfward in winter? *Ocean Dynamics*, *60*(2), 413–426. https://doi.org/10.1007/s10236-009-0259-5

Pedlosky, J. (1979). *Geophysical fluid dynamics* (p. 624). Springer-Verlag.

Pedlosky, J. (1996). *Ocean circulation theory* (p. 453). Springer-Verlag.

Peliz, A., Dubert, J. S., & Haidvogel, D. B. (2003). Subinertial response of a density-driven eastern boundary poleward current to wind forcing. *Journal of Physical Oceanography*, *33*(8), 1633–1650. https://doi.org/10.1175/2415.1

Qiu, B., & Imasato, N. (1990). A numerical study on the formation of the Kuroshio counter current and the Kuroshio branch current in the East China Sea. *Continental Shelf Research*, *10*(2), 165–184. https://doi.org/10.1016/0278-4343(90)90028-K

Qiu, B., Toda, T., & Imasato, N. (1990). On Kuroshio front fluctuations in the East China Sea using satellite and in situ observational data. *Journal of Geophysical Research*, *95*(C10), 18191–18204. https://doi.org/10.1029/JC095iC10p18191

Rhines, P. (1983). Lectures in geophysical fluid dynamics. *Lectures in Applied Mathematics*, *20*, 3–58.

Shchepetkin, A. F., & McWilliams, J. C. (2003). A method for computing horizontal pressure-gradient force in an oceanic model with a nonaligned vertical coordinate. *Journal of Geophysical Research*, *108*(C3), 3090. https://doi.org/10.1029/2001JC001047

Shchepetkin, A. F., & McWilliams, J. C. (2005). The regional oceanic modeling system (ROMS): A split-explicit, free-surface, topography-following-coordinate oceanic model. *Ocean Modelling*, *9*(4), 347–404. https://doi.org/10.1016/j.ocemod.2004.08.002

Song, Y., & Haidvogel, D. (1994). A semi-implicit ocean circulation model using a generalized topography-following coordinate system. *Journal of Computational Physics*, *115*(1), 228–244. https://doi.org/10.1006/jcph.1994.1189

Stommel, H. (1958). The abyssal circulation. *Deep-Sea Research*, *5*(1), 80–82. https://doi.org/10.1016/S0146-6291(58)80014-4

Stommel, H., & Arons, A. B. (1960a). On the abyssal circulation of the world ocean. I. Stationary planetary flow patterns on a sphere. *Deep-Sea Research*, *6*, 140–154. https://doi.org/10.1016/0146-6313(59)90065-6

Stommel, H., & Arons, A. B. (1960b). On the abyssal circulation of the world ocean. II. An idealized model of the circulation pattern and amplitude in oceanic basins. *Deep-Sea Research*, *6*, 217–233. https://doi.org/10.1016/0146-6313(59)90065-6

Sugimoto, T., Kimura, S., & Miyaji, K. (1988). Meander of the Kuroshio front and current variability in the East China Sea. *Journal of the Oceanographical Society of Japan*, *44*(3), 125–135. https://doi.org/10.1007/BF02302619

Toole, J. M., Andres, M., Le Bras, I. A., Joyce, T. M., & McCartney, M. S. (2017). Moored observations of the deep western boundary current in the NW Atlantic: 2004–2014. *Journal of Geophysical Research: Oceans*, *122*(9), 7488–7505. https://doi.org/10.1002/2017JC012984

Warren, B. A., & Speer, K. G. (1991). Deep circulation in the eastern south Atlantic Ocean. *Deep-Sea Research, Part A: Oceanographic Research Papers*, *38*(S1), S281–S322. https://doi.org/10.1016/S0198-0149(12)80014-8

Wei, Y. (2018). Cross-shelf circulation induced by the Kuroshio shear stress in the East China Sea. *Journal of Physical Oceanography*, *48*(7), 1479–1493. https://doi.org/10.1175/JPO-D-17-0204.1

Yanagi, T., Shimuzu, T., & Lie, H. (1998). Detailed structure of the Kuroshio frontal eddy along the shelf edge of the East China Sea. *Continental Shelf Research*, *18*(9), 1039–1056. https://doi.org/10.1016/S0278-4343(98)80005-8

Yang, D., Huang, R., Feng, X., Qi, J., Gao, G., & Yin, B. (2020). Wind stress over the Pacific Ocean east of Japan drives the shelf circulation east of China. *Continental Shelf Research*, *201*, 104122. https://doi.org/10.1016/j.csr.2020.104122

Yang, D., Huang, R., Yin, B., Feng, X., Chen, H., Qi, J., et al. (2018). Topographic beta spiral and onshore intrusion of the Kuroshio Current. *Geophysical Research Letters*, *45*(1), 287–296. https://doi.org/10.1002/2017GL076614

Yang, D., Yin, B., Chai, F., Feng, X., Xue, H., Gao, G., & Yu, F. (2018). The onshore intrusion of Kuroshio subsurface water from February to July and a mechanism for the intrusion variation. *Progress in Oceanography*, *167*, 97–115. https://doi.org/10.1016/j.pocean.2018.08.004

Yang, J. (2005). The arctic and subarctic ocean flux of potential vorticity and the arctic ocean circulation. *Journal of Physical Oceanography*, *35*(12), 2387–2407. https://doi.org/10.1175/JPO2819.1

Yang, J., & Price, J. F. (2000). Water-mass formation and potential vorticity balance in an abyssal ocean circulation. *Journal of Marine Research*, *58*(5), 789–808. https://doi.org/10.1357/002224000321358918

Yang, J., & Price, J. F. (2007). Potential vorticity constraint on the flow between two basins. *Journal of Physical Oceanography*, *37*(9), 2251–2266. https://doi.org/10.1175/JPO3116.1

Zhang, J., Zhao, L., Guo, X., Miyazawa, Y., & Sun, Q. (2017). Water exchange across isobaths over the continental shelf of the East China Sea. *Journal of Physical Oceanography*, *47*(5), 1043–1060. https://doi.org/10.1175/JPO-D-16-0231.1

Zhu, Y., Sun, J., Wang, Y., Wei, Z., Yang, D., & Qu, T. (2017). Effect of potential vorticity flux on the circulation in the South China Sea. *Journal of Geophysical Research: Oceans*, *122*(8), 6454–6469. https://doi.org/10.1002/2016JC012375

Zhu, Y., Wang, L., Wang, Y., Xu, T., Li, S., Cao, G., et al. (2019). Stratified circulation in the Banda Sea and its causal mechanism. *Journal of Geophysical Research: Oceans*, *124*(10), 7030–7045. https://doi.org/10.1029/2019JC015279